Cellular/Molecular

# An Angstrom Scale Interaction between Plasma Membrane ATP-Gated $P2X_2$ and $\alpha_4\beta_2$ Nicotinic Channels Measured with Fluorescence Resonance Energy Transfer and Total Internal Reflection Fluorescence Microscopy

**Baljit S. Khakh,[1] James A. Fisher,[1] Raad Nashmi,[2] David N. Bowser,[1] and Henry A. Lester[2]**

[1]Medical Research Council Laboratory of Molecular Biology, Cambridge CB2 2QH, United Kingdom, and [2]Division of Biology, California Institute of Technology, Pasadena, California 91125

**Structurally distinct nicotinic and P2X channels interact functionally, such that coactivation results in cross-inhibition of one or both channel types. It is hypothesized, but not yet proven, that nicotinic and P2X channels interact at the plasma membrane. Here, we show that plasma membrane $\alpha_4\beta_2$ nicotinic and $P2X_2$ channels form a molecular scale partnership and also influence each other when coactivated, resulting in nonadditive cross-inhibitory responses. Total internal reflection fluorescence and fluorescence resonance energy transfer microscopy between fluorescently labeled $P2X_2$ and $\alpha_4\beta_2$ nicotinic channels demonstrated close spatial arrangement of the channels in human embryonic kidney cells and in hippocampal neuron membranes. The data suggest that $P2X_2$ and $\alpha_4\beta_2$ channels may form a dimer, with the channels ~80 Å apart. The measurements also show that $P2X_2$ subunits interact specifically and robustly with the $\beta_2$ subunits in $\alpha_4\beta_2$ channels. The data provide direct evidence for the close spatial apposition of full-length $P2X_2$ and $\alpha_4\beta_2$ channels within 100 nm of the plasma membrane of living cells.**

*Key words:* **channel; cholinergic; purinergic; acetylcholine receptor; ACh; fluorescence microscopy; P2X**

## Introduction

Transmitter-gated ion channels are found in neurons and synapses, where they bind neurotransmitter and convert this presynaptic chemical signal into a postsynaptic signaling event (Hille, 2001). Mammalian transmitter-gated ion channels consist of three families: Cys-loop channels for ACh, GABA, glycine, and serotonin; glutamate-gated channels (kainate, AMPA, and NMDA); and the ATP-gated P2X channels (Green et al., 1998; Khakh, 2001; Lester et al., 2004), of which seven subunits are known ($P2X_1$–$P2X_7$). There is little sequence, topological or structural similarity between members of the Cys-loop, glutamate-gated, and P2X channel family members (North, 1996a,b), leading to the assumption that they act independently in neurons and synapses.

Motivated by pioneering work on neurons showing that P2X and nicotinic channels may not act independently (Nakazawa, 1994; Barajas-Lopez et al., 1998; Searl et al., 1998; Zhou and Galligan, 1998), we suggested that neuronal nicotinic and P2X channels undergo cross-inhibitory functional interactions because of conformational coupling akin to conformational spread (Khakh et al., 2000). Conformational spread has been proposed as a general mechanism for signal integration by cells (Bray and Duke, 2004): conformational changes in one protein are relayed to its neighbors because of close spatial interactions. Cross-inhibition also occurs for P2X, nicotinic, GABA, and 5-$HT_3$ subunits in heterologous expression studies as well as for natively expressed channels in neurons and synapses (Barajas-Lopez et al., 1998; Searl and Silinsky, 1998; Searl et al., 1998; Zhou and Galligan, 1998; Khakh et al., 2000; Sokolova et al., 2001b; Barajas-Lopez et al., 2002; Boue-Grabot et al., 2003, 2004a,b). One functional measure of cross-inhibition between ATP-gated P2X and ACh-gated nicotinic channels is that coapplication of ATP and ACh to cells expressing these channels evokes responses smaller than the sum of the individual ATP and ACh-evoked currents (Searl and Silinsky, 1998). This lack of summation implies that, when P2X and nicotinic channels are simultaneously activated, fewer channels open than expected if one assumes that the two channel populations function independently. The underlying mechanisms responsible for cross-inhibition between $P2X_2$ and nicotinic channels remain incompletely understood.

If conformational spread is the cause of cross-inhibition between $P2X_2$ and nicotinic channels, a close spatial arrangement between the channels in the plasma membrane is expected (Bray

Received Feb. 10, 2005; revised June 13, 2005; accepted June 14, 2005.

Research in our laboratories is supported by the Medical Research Council (MRC), the European Molecular Biology Organization, the Human Frontiers Science Program, and National Institutes of Health Grants NS11756 and DA17279. J.A.F. was supported by an MRC Studentship, R.N. was supported by a postdoctoral fellowship from the California Tobacco-Related Disease Research Program and the Elizabeth Ross Fund, and D.N.B. was supported in part by a European Molecular Biology Organization Fellowship. We thank Julian Revie for constructing some of the nicotinic ACh receptor cDNAs. Requests for cDNAs should be addressed to Baljit S. Khakh (bsk@mrc-lmb.cam.ac.uk) and Henry A. Lester (lester@caltech.edu).

Correspondence should be addressed to Baljit S. Khakh, Medical Research Council Laboratory of Molecular Biology, Hills Road, Cambridge CB2 2QH, UK. E-mail: bsk@mrc-lmb.cam.ac.uk.

DOI:10.1523/JNEUROSCI.0561-05.2005

 0270-6474/05/256911-10$15.00/0

and Duke, 2004) but has remained unproven. We took advantage of recent data demonstrating that both $P2X_2$ and $\alpha_4\beta_2$ channels can be innocuously labeled with GFP-based fluorophores in their cytosolic domains (Khakh et al., 2001; Nashmi et al., 2003; Fisher et al., 2004). We first asked whether channels formed by these brain-expressed subunits ($P2X_2$, $\alpha_4$, $\beta_2$) (Kanjhan et al., 1999; Labarca et al., 2001; Fonck et al., 2003) show cross-inhibition similar to that demonstrated for channels found in the peripheral nervous system, and we then used fluorescence resonance energy transfer (FRET) microscopy to probe interactions between $P2X_2$ and $\alpha_4\beta_2$ channels in the plasma membrane of single cells.

## Materials and Methods

*Molecular biology.* cDNAs for wild-type (wt) $P2X_2$, $\alpha_4$, and $\beta_2$ subunits, as well as cyan fluorescent protein (CFP)- and yellow fluorescent protein (YFP)-labeled $P2X_2$ ($P2X_2$-C, $P2X_2$-Y), $\alpha_4$ subunits ($\alpha_4$-Y, $\alpha_4$-C), and $\beta_2$ subunits ($\beta_2$-C, $\beta_2$-Y) were used (where C is CFP, and Y is YFP). These were all available from previous work (Nashmi et al., 2003; Fisher et al., 2004). For the generation of $P2X_6$-C and $P2X_6$-Y, the starting vectors were $P2X_2$-C and $P2X_2$-Y. In these vectors, *Hin*dIII (5′) and *Xho*I (3′) digestion yielded $P2X_2$. By PCR (PCR Core kit; Qiagen, Crawley, UK) the $P2X_6$ coding region was amplified (no stop codon) with noncoding 5′ *Hin*dIII and in frame 3′ *Xho*I sites, using plasmids encoding $P2X_6$ as template (Khakh et al., 1999). These PCR products were cloned into *Hin*dIII and *Xho*I sites of $P2X_2$-C and $P2X_2$-Y to generate $P2X_6$-C and $P2X_6$-Y, respectively. All constructs were sequenced (Lark Technologies, Saffron Walden, UK or MRC Gene Service, Cambridge, UK).

*Human embryonic kidney cell culture and transfection.* Human embryonic kidney 293 (HEK 293) cells (obtained from American Type Culture Collection via LGC Promochem, Teddington, UK) were maintained in 75 $cm^2$ cell culture flasks (Corning; Fisher Scientific, Loughborough, UK) in DMEM/Ham's F-12 media with Glutamax (Invitrogen, Paisley, UK) supplemented with 10% fetal bovine serum and penicillin/streptomycin. Cells were grown in a humidified atmosphere of 95% air/5% $CO_2$ at 37°C in a cell culture incubator. The cells were split 1 in 10 when confluence reached 60–90%, which was generally every 3–4 d. Cells were prepared for transfection by plating onto six-well plates at the time of splitting, 3–4 d before transfection. They were transfected at 60–90% confluence. For transient expression in HEK 293 cells, we used 0.5–1 $\mu$g of plasmid cDNA and the Effectene transfection reagent (Qiagen) for each well of a six-well plate. The manufacturer's instructions were followed, with 4 $\mu$l of enhancer and 10 $\mu$l of Effectene used for each transfection. The transfection efficiency was 40–60%. For the functional measurements of cross-inhibition between $P2X_2$ and $\alpha_4\beta_2$ channels, we used a previously available stable cell line expressing $\alpha_4\beta_2$ channels (Egan and Khakh, 2004), which has been described in detail previously (Chavez-Noriega et al., 2000), and transfected subunit cDNAs using procedures described above. All recordings were made 1–2 d after transfection, as described below. For FRET experiments, we used wild-type HEK cells and transfected cDNAs for wt $\alpha_4$, $\alpha_4$-Y, $\alpha_4$-C, wt $\beta_2$, $\beta_2$-Y, $\beta_2$-C, $P2X_2$-Y, and $P2X_2$-C subunits in all combinations, as appropriate (see Results and Table 1). Using this approach, we tested all possible partnerships between $\alpha_4\beta_2$ and $P2X_2$ channels with FRET (see Results) in a cell type otherwise devoid of $\alpha_4\beta_2$ or $P2X_2$ channels, thus avoiding the complication of nontagged subunits to FRET.

*Hippocampal neuron culture and transfection.* Typically five rat pups at embryonic day 19 (E19) were used for hippocampal cultures. The mother was killed following Home Office (London, UK) and local procedures, and the embryos were removed to ice-cold dissection medium comprising Earle's buffered salt solution (with no $Ca^{2+}$ or $Mg^{2+}$ and no phenol red; Invitrogen), HEPES (10 mM, pH 7.4; Sigma, Poole, UK), and penicillin/streptomycin (1:100 dilution; Invitrogen). Hippocampi were dissected in Petri dishes filled with ice-cold medium. The dissected hippocampi (in medium, on ice) were cut in half, transferred to a 15 ml tube with 10 U/ml papain PAP2 powder [Worthington Biochemical (Lakewood, NJ) PAPAIN-022], and incubated for 15 min at 37°C. When the pieces of tissue had settled, digestion solution was removed and 10 ml of cold culture medium was added. This step was repeated, and the pieces were triturated five to six times in a 2 ml volume of ice-cold culture medium with paired flame-polished pipettes of progressively smaller bores. A hemacytometer was used to quantify yield (typically 2.5 million/ml), and ~200,000 neurons were used for plating onto each coverslip. The coverslips were precoated with poly-D-lysine (50 $\mu$g/ml; Sigma) and then overnight with 150 $\mu$l of 20 $\mu$g/ml laminin (Sigma) in sterile dissection medium. Three hours after plating, the cells were fed with 2 ml of prewarmed culture medium and fed again 1 d after plating by substituting 1 ml of fresh prewarmed medium for 1 ml of existing medium. Cells were then fed every 4–5 d and used for experiments after 14 d *in vitro*. The culture medium comprised MEM with no phenol red (Invitrogen), glucose (20 mM), penicillin/streptomycin (Invitrogen), Na pyruvate (2 mM; Sigma), HEPES (25 mM; Sigma), N2 supplement (1:100 dilution; Invitrogen), and heat-inactivated horse serum (10%; Invitrogen). Effectene transfection reagent was used to transfect 0.5–1.0 $\mu$g of the appropriate cDNA per well of a six-well plate, which contained 3–4 coverslips. The instructions of the manufacturer were followed, except that 8 $\mu$l of enhancer and 24 $\mu$l of Effectene were used per 1 $\mu$g of cDNA. Experiments were performed 1–2 d after transfection, when transfection was successful typically in 1–2% of cells.

*Midbrain mesencephalic dopaminergic neuron cultures and transfection.* Ventral mesencephalic neuronal cultures were prepared as described previously (Nashmi et al., 2003). Brain tissue containing primary mesencephalic neurons of the ventral tegmental area from E14 BDF1 mouse embryos (Shimoda et al., 1992) was incubated in plating medium (Neurobasal, 2% B27, 0.5 mM Glutamax, and 5% horse serum) with 1 mg/ml papain at 37°C for 20 min. The digested tissue was mechanically dispersed, laid on 4% bovine serum albumin (Fraction V; Sigma, St. Louis, MO) in PBS, centrifuged for 6 min at 300 × *g* and resuspended in plating medium. Cells (~150,000) were plated onto 35 mm culture dishes with 10-mm-diameter glass coverslip bottoms (MatTek, Ashland, MA) that were coated with poly-DL-lysine (catalog #P9011; 1 mg/ml; Sigma, St. Louis, MO) dissolved in sterile water. To transfect one dish of neurons, 1 $\mu$g of each cDNA was mixed with 60 $\mu$g of Nupherin-neuron (Biomol Research Laboratories, Plymouth Meeting, PA) in 400 $\mu$l of Neurobasal medium without phenol red. Lipofectamine 2000 (3 $\mu$l; Invitrogen, Carlsbad, CA) was mixed in 400 $\mu$l of Neurobasal media. The two solutions were incubated for 15 min at room temperature, combined, and incubated for another 45 min at room temperature. The medium of the mesencephalic cultures was replaced with plating medium without added serum, and the transfection medium was added. The culture dishes were centrifuged at 100 × *g* for 5 min on a swinging bucket rotor and incubated for 30 min at 37°C. Then, the transfection mixture was removed and replaced with the original plating medium. Experiments were performed 2 d after transfection, when transfection was typically successful in 1–2% of cells.

*Electrophysiology.* HEK 293 cells were used for recordings 24–48 h after transfection, as described previously (Fisher et al., 2004). The cells were gently mechanically dispersed and plated onto glass coverslips 2–12 h before use. We included this step to ensure that the cells became spherical and therefore adequately space clamped during recordings (Egan et al., 1998). The extracellular recording solution comprised (in mM) 147 NaCl, 2 KCl, 1 $MgCl_2$, 1 $CaCl_2$, 10 HEPES, and 10 glucose, pH 7.4, and the pipette solution comprised (in mM) 154 KCl (or CsCl), 11 EGTA, and 10 HEPES. Whole-cell voltage-clamp recordings were made with 5 MΩ borosilicate glass electrodes (World Precision Instruments, Stevenage, UK), using an Axopatch 1D amplifier controlled by a computer running pClamp 8.1 software via a Digidata 1322 interface (Molecular Devices, Union City, CA). Data were filtered at 0.5–2 kHz and digitized at 1–5 kHz. Agonists were applied for 0.2–4 s at 2–3 min intervals using triple-barreled theta-glass (Egan and Khakh, 2004) and a rapid solution changer system (Perfusion Fast-Step System SF-77; Warner Instruments, Hamden, CT). Voltage ramps (0.5 s duration; −120 to +60 mV) were applied at the peak response to each agonist.

*Confocal FRET microscopy.* Confocal FRET imaging of midbrain neurons has been described previously (Nashmi et al., 2003). Cultured and transfected mesencephalic neurons were visualized at room temperature in extracellular buffer comprising (in mM) 150 NaCl, 4 KCl, 2 $CaCl_2$, 2 $MgCl_2$, 10 HEPES, 10 D-glucose, and 1 ascorbic acid, pH 7.4. Ascorbic

acid was included to minimize damage to dendrites during photodestruction. A series of λ-stack *x–y* images were collected from an upright LSM 510 Meta laser-scanning confocal microscope using an Achroplan IR 63× 0.9 numerical aperture (NA) water-immersion objective (Zeiss, Oberkochen, Germany). Images were collected over a spectral range between 462.9 and 602 nm with bandwidths of 10.7 nm after excitation of CFP with the 458 nm laser line of an argon laser. Pinhole was 1.32 Airy units, and the *Z* resolution was ~2.0 μm. Images were collected at a 12-bit intensity resolution over 512 × 512 pixels at a pixel dwell time of 12.8 μs. FRET was recorded by examining the dequenching of CFP after incremental photodestruction of YFP by the 514 nm argon laser line. λ Stacks were acquired at various time points before and after photodestruction of YFP. These time points included 0, 0.13, 0.26, 0.52, 1.05, 1.57, 2.09, and 6.81 min. We separated the fluorescence contribution of each fluorescent protein (CFP or YFP) using a linear unmixing algorithm based on the spectral signatures of YFP and CFP created from reference λ-stack images of cells expressing either soluble YFP or soluble CFP, respectively. These unmixed YFP and CFP images (Dickinson et al., 2001; Lansford et al., 2001) were analyzed for FRET efficiency. Background fluorescence for both CFP and YFP, determined as the mean fluorescence intensity from an area containing cells that did not express the constructs, was subtracted from the overall intensity. Mean fluorescence intensities of CFP and YFP were determined by tracing the outer perimeter of the cell, the neuronal soma, or dendrite with a region of interest. However, in the case of FRET calculated for cell membrane surface receptors, mean fluorescence intensity was calculated for only the outer ~2 μm shell of fluorescence and did not include the cell interior.

*Epifluorescence FRET microscopy.* We used an Olympus (Southall, UK) BX50 microscope equipped with a Peltier-cooled (−15°C) half-inch interline transfer chip Imago CCD camera (640 × 480 pixels; each pixel, 9.9 × 9.9 μm), epifluorescence condenser (Olympus IX two-port flash/imaging condenser), control unit (containing ISC and PDC boards), and the Polychrome IV monochromator (all from TILL Photonics, Gräfelting, Germany). The light from the monochromator was led to the microscope through a quartz fiber light guide. The hardware was controlled by a personal computer, an appropriate frame grabber (TILL Photonics), and macros driven by TILLvisION version 3.3 software. The cells were viewed with a 40× water-immersion objective lens with a numerical aperture of 0.8 (Olympus). We used the following filters for acquiring CFP or YFP images (in nm; all from Glen Spectra, Stanmore, UK): CFP (dichroic, 455DRLP; emitter, 480AF30) and YFP (dichroic, 525DRLP; emitter, 545AF35). To photodestroy the YFP, we used 525 nm light from the monochromator, and a 525DRLP dichroic. FRET was determined as described below.

*Total internal reflection fluorescence microscopy and FRET.* Briefly, we used an Olympus IX70 microscope equipped with a Princeton Instruments (Trenton, NJ) cooled I-PentaMAX camera with High Blue Gen III Intensifier (Roper Scientific, Trenton, NJ). The control of excitation and image acquisition was achieved using MetaMorph software and drivers (Universal Imaging, Marlow, UK) and shutters, filter wheels, and Proscan II control box (Prior Scientific, Cambridge, UK). The beams of 488/515 nm Ar (150 mW) and 442 nm He-Cd (12.5 mW) lasers (Melles Griot, Carlsbad, CA) at <5% power (constant for all experiments reported) were combined and controlled with an IX2-COMB (Olympus), Uniblitz shutters (Prior Scientific) and acousto-optical tunable filter and controller (AA Optoelectronics, Les Chevreuse, France) and fed into a fiber optic (FV5-FUR; Olympus) for entry into the total internal reflection fluorescence microscopy (TIRF) condenser (IX2-RFAEVA-2; Olympus). Cells were plated onto glass-bottom Petri dishes (170 μm thick; Willco Wells, Amsterdam, The Netherlands) 24–48 h before imaging and were viewed with a 60× oil-immersion objective lens, NA 1.45 (Olympus). FRET was determined with donor dequenching. During donor dequenching experiments on the TIRF rig, we noted that significant photodestruction of YFP occurred within ~10 s, versus many minutes for epifluorescence imaging (Fisher et al., 2004). This difference, likely reflecting the use of different microscopes (IX70 vs BX50), objective lenses (60×, NA 1.45 vs 40×, NA 0.8), and light sources (laser vs xenon lamp), implied that, for TIRF experiments, we would obtain only a single time point for donor dequenching (see below, Data analysis and Results). The camera gain was adjusted for maximum signal-to-noise for each cell and kept constant for all image acquisitions of a particular cell.

*Data analysis.* For donor dequenching experiments, the FRET efficiency (*e*) was calculated as follows:

$$e = (1 - [I_{\text{C-before}}/I_{\text{C-after}}]) \times 100\,, \quad (1)$$

where $I_{\text{C-before}}$ is the donor fluorescence intensity before photodestruction, and $I_{\text{C-after}}$ is the intensity after photodestruction. The photodestruction of the YFP proceeds with a rate equivalent to the dequenching of the donor, and plotting the photorecovery versus photodestruction yields a straight line (see Fig. 1). We used such linear plots and extrapolated to 100% acceptor photodestruction to calculate the maximum donor dequenching for epifluorescence microscopy (see Fig. 1): *e* is given by the *y*-axis intercept. For TIRF microscopy, we estimated FRET *e* from a single time point when the acceptor was ~85% destroyed and extrapolated to 100% destruction by constraining the linear regression to pass through the origin. This was the most appropriate tactic, because it was not possible to track time-dependent photodestruction with TIRF: on one hand, as noted, the bleaching occurred too rapidly with laser illumination (<0.5–1 min). In contrast, with epifluorescence illumination, bleaching typically took ~30 min, allowing multiple evenly spaced time points to be collected accurately (see Results) (Fisher et al., 2004); however, because during TIRF only the plasma membrane within 100 nm of the glass–cell interface, the footprint, is illuminated (Steyer and Almers, 2001), it is necessary to destroy the acceptor fluorophore rapidly within this region and to measure donor dequenching before channels that are not within the evanescent field of illumination (and therefore neither destroyed or dequenched) can either diffuse or be inserted into the footprint. Thus, the fact that for TIRF microscopy maximal photodestruction occurred rapidly was a fortuitous feature that enabled us to determine FRET from a single time point. In Results, we present a detailed comparison of FRET values determined for a single time point versus those calculated from multiple time points.

To approximate distances, we used the Förster equation:

$$e = \frac{R_0^6}{R_0^6 + R^6}\,, \quad (2)$$

where

$$R_0^6 = (8.79 \times 10^{23})\kappa^2 n^{-4} \phi_{\text{D}} J_{\text{DA}} \quad (3)$$

*e* is the experimentally determined FRET efficiency, and *R* is the distance between donor and acceptor fluorophores (Michalet et al., 2003; Bunt and Wouters, 2004). $R_0$ includes terms for the donor quantum efficiency ($\phi_{\text{D}}$), the solvent refractive index (*n*), overlap of the donor emission and acceptor absorption spectra ($J_{\text{DA}}$), and the orientation factor ($\kappa^2$). $R_0$ is the distance at which *e* is 50% for any given fluorophore pair. In the case of CFP and YFP, this is 49.2 Å (Patterson et al., 2000) or 50.4 Å (Tsien, 1998). We have no good reason to choose between these values and have taken the average and rounded to the nearest whole number to give a value of 50 Å (5 nm). Importantly, $R_0$ contains a term for the fluorophore dipole orientation factor ($\kappa^2$), which, at 2/3, assumes random tumbling of the fluorophores (Bunt and Wouters, 2004). This means that $R_0$ and the distance measurements reported here assume that the fluorophores adopt all spherically random orientations. Given that we do not know the relative orientation of the fluorophores on $P2X_2$ and nicotinic channels, assuming a $\kappa^2$ value of 2/3 seems parsimonious and appropriate (Michalet et al., 2003; Bunt and Wouters, 2004) and is supported by empirical data for CFP and YFP fused to the cytosolic C termini of inwardly rectifying $K^+$ channels (Riven et al., 2003), which have a membrane topology similar to P2X channels (North, 1996a). When interpreting FRET efficiency measurements in terms of distance, it is important to consider that, in the case of CFP and YFP, the fluorophore is buried in the center of a β-can 30 Å in width and 45 Å in length (Tsien, 1998). An additional consideration is that we do not know the absolute ratio of donors to acceptors during FRET at the single molecule level (see Discussion).

For the FRET experiments, we chose regions of interest (ROIs) *post hoc* (Fisher et al., 2004). Our criteria were that ROIs (1) were bright in both

CFP and YFP images, (2) were located at the edge, presumably plasma membrane of the cell, (3) did not change or drift in intensity during the control period, and (4) remained in focus during the entire experiment.

For the electrophysiological experiments, we used analysis that has been described previously (Khakh et al., 2000). Briefly, we measured the currents activated by ATP ($I_{ATP}$), ACh ($I_{ACh}$), and ATP and ACh together ($I_{ATP/ACh}$). From these, we calculated the predicted current ($I_{Predicted}$) and the occluded current ($I_{Lost}$) on a cell-by-cell basis, where

$$I_{Predicted} = I_{ACh} + I_{ATP}, \quad (4)$$

$$I_{Lost} = I_{Predicted} - I_{ATP/ACh}. \quad (5)$$

Thus, the percentage contribution of any one component such as $I_{ACh}$ to the predicted current can be calculated as $(I_{ACh}/I_{Predicted}) \times 100$. Rectification index was calculated as the ratio of macroscopic slope conductances at voltages ±40 mV from the reversal potential. Reversal potentials were measured using two- or three-order polynomial fits to the current–voltage relationships and were taken as the values at which the fitted line first intersected the *x*-axis (see Fig. 1*C*, bottom). Electrophysiological analysis was performed with Clampfit (Molecular Devices) or Origin 6.1 (OriginLab, Northampton, MA), and all statistical tests were run in GraphPad Instat 3.0 (GraphPad Software, San Diego, CA). Image analysis was performed with ImageJ (http://rsb.info.nih.gov/ij/). Data in the text and graphs are shown as mean ± SEM from *n* determinations as indicated.

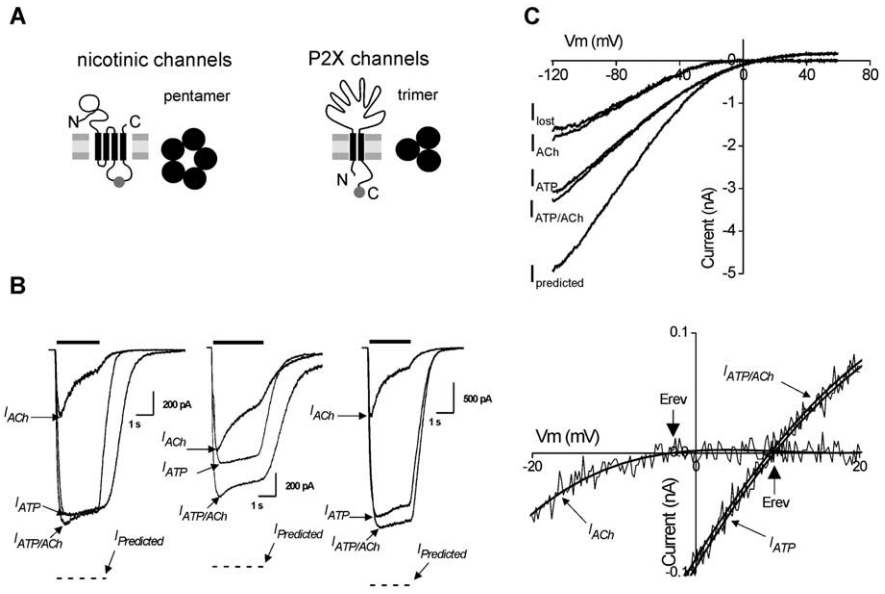


**Figure 1.** Cross-inhibition between $P2X_2$ and $\alpha_4\beta_2$ channels expressed in HEK cells. ***A***, Diagram of presently understood membrane topology and oligomeric state of nicotinic and P2X channels. N, N terminus; C, C terminus. ***B***, Three examples of inward currents (−60 mV) evoked by sequential ~5 s applications of ATP, ACh, and ATP/ACh from an HEK cell expressing $P2X_2$ and $\alpha_4\beta_2$ channels (for average data, see Results). The dashed line indicates the level of the peak predicted current if there was no cross-inhibition. ***C***, Top, Representative current–voltage relationships of currents evoked by ATP, ACh, and ATP/ACh together (for average data, see Results). Bottom, Expanded plot near the reversal potential (Erev) for the current–voltage relationships shown in the top panel. The thin lines are the raw data, and the thick lines are two- or three-order polynomial fits to the data (see Materials and Methods, Data analysis). In all cases, agonists (100 μM) were applied at 2 min intervals.

## Results

### Electrophysiological evidence for cross-inhibition between $P2X_2$ and $\alpha_4\beta_2$ channels

We applied ATP (100 μM) to activate $P2X_2$ and ACh (100 μM) to activate nicotinic channels in HEK cells coexpressing wt $P2X_2$ and $\alpha_4\beta_2$ channels (Fig. 1*A*,*B*). We measured robust ATP- and ACh-evoked inward currents (at −60 mV: $I_{ATP}$ at −1161 ± 311 pA and $I_{ACh}$ at −522 ± 113 pA; $n = 9$) when either agonist was applied alone, but less than the predicted ($I_{Predicted}$ at −1635 ± 402 pA; $n = 9$) current when both ACh and ATP were coapplied ($I_{ATP/ACh}$) (Fig. 1*B*). The measured current ($I_{ATP/ACh}$ at −1037 ± 265 pA; $n = 9$) on coapplication of ATP and ACh was consistently smaller than the predicted current by 39 ± 4% ($I_{Lost}$). This $I_{Lost}$ percentage was thus approximately equal to the $I_{ACh}$ percentage (35 ± 3%) and significantly smaller than the $I_{ATP}$ percentage (70 ± 2%), where 100% equals $I_{predicted}$ (see Materials and Methods, Data analysis). Interestingly, the rectification indices and reversal potentials of $I_{ATP/ACh}$ (0.18 ± 0.03 and +6.6 ± 0.6 mV; $n = 5$) were similar to those of $I_{ATP}$ (0.21 ± 0.02 and +7.5 ± 0.9 mV; $n = 5$) and significantly different from $I_{ACh}$ (0.04 ± 0.02 and −5.4 ± 1.0 mV; $n = 5$) (Fig. 1*C*), as though few nicotinic channels opened after coapplication of ATP and ACh. Together, these data extend previous work on peripheral nervous system channels (see Introduction) to $\alpha_4\beta_2$ nicotinic and $P2X_2$ channels abundantly found in the brain (Kanjhan et al., 1999; Labarca et al., 2001; Fonck et al., 2003).

### FRET between $P2X_2$ and $\alpha_4\beta_2$ channels in HEK 293 cells

We used the donor dequenching method (Michalet et al., 2003) to estimate FRET efficiency for $P2X_2$ and $\alpha_4\beta_2$ channels expressed in HEK 293 cells (Fig. 2*A*). If FRET occurs, one expects full removal (photodestruction) of the YFP acceptor to increase CFP fluorescence by a percentage amount that is equal to FRET *e*. We determined this value by plotting the photorecovery of CFP as a function of the photodestruction of YFP and estimated *e* when we extrapolated the data to 100% YFP photodestruction for a membrane ROI (Fig. 2*B–E*). Our values of *e* for $P2X_2$-C/$P2X_2$-Y and $\alpha_4$-Y/$\beta_2$-C channels (Table 1, 28% and 25%, respectively) agree with previous work (Nashmi et al., 2003; Fisher et al., 2004). The 10% difference between $\alpha_4$-Y/$\beta_2$-C ($e = 25\%$) and $\alpha_4$-C/$\beta_2$-Y ($e = 34\%$) (Table 1, Fig. 2) may reflect a preferential $\alpha_4$:$\beta_2$ stoichiometric ratio of 2:3 in the heteromeric nicotinic channels (Table 1).

Importantly, we also measured strong FRET between CFP- or YFP-labeled $P2X_2$ and $\alpha_4\beta_2$ channels under some conditions. FRET between $P2X_2$ and $\alpha_4\beta_2$ was strong when the cognate acceptor or donor fluorophore was on the $\beta_2$ subunit ($e = 23$ and 26%) (Table 1, Fig. 2*D*) but was weak or absent when the acceptor ($e = 10\%$) or donor ($e = 0\%$) fluorophores were on the $\alpha_4$ subunit (Table 1, Fig. 2*E*). However, we know that the $P2X_2$–$\beta_2$ interaction does require assembled $\alpha_4\beta_2$ channels, because no FRET was measured from cells expressing CFP-labeled $P2X_2$ channels and YFP-labeled $\beta_2$ subunits ($e = \sim 0\%$; $n = 9$) (Table 1). These data demonstrate that (1) $P2X_2$ and $\alpha_4\beta_2$ channels were spatially close and that (2) FRET is stronger for $P2X_2$ and $\beta_2$ than for $P2X_2$ and $\alpha_4$.

We next repeated the experiments with TIRF–FRET microscopy (Fisher et al., 2004). This method allows for the visualization of channels within ~100 nm of the plasma membrane (Fig. 3*A*) in an area called the footprint (Steyer and Almers, 2001). We used donor dequenching to estimate FRET *e*. Figure 3*B* shows donor and acceptor images from cell footprints expressing $P2X_2$-C/$P2X_2$-Y, $\alpha_4$-C/$\beta_2$-Y, and $P2X_2$-C/$\alpha_4\beta_2$-Y subunits before and af-

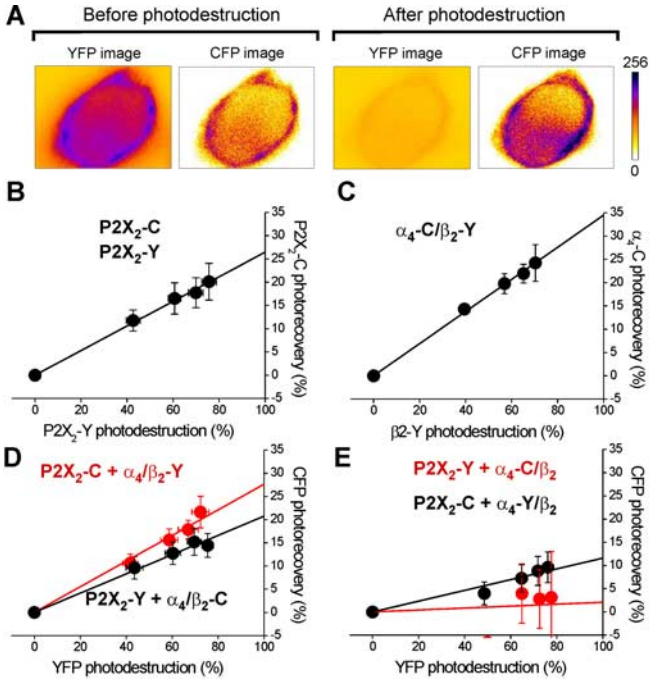


**Figure 2.** FRET between $P2X_2$ and $\alpha_4\beta_2$ channels in HEK cells. ***A***, Donor (CFP) and acceptor (YFP) images of HEK cells expressing $\alpha_4$-C/$\beta_2$-Y channels before and after photodestruction of the acceptor fluorophore. ***B***, Linear plots of donor (CFP) photorecovery versus acceptor (YFP) photodestruction for channels formed by coexpressing $P2X_2$-C and $P2X_2$-Y channels. The *y*-axis intercept is a measure of FRET *e* (see Materials and Methods, Data analysis). ***C–E***, As in ***B*** but for channels formed by coexpressing the indicated subunits. ***B–E***, Linear plots for membrane ROI only, whereas Table 1 shows data from whole-cell ROI as well. Error bars represent SEM.

ter acceptor photodestruction. From images such as these, we calculated FRET *e* by extrapolating to 100% acceptor photodestruction (Fig. 4*A*) for equally sized footprints (Fig. 4B). In contrast to the experiments with epifluorescence microscopy (Fig. 2*B*,*C*), we could obtain only one time point, at ~85% acceptor photodestruction (see Materials and Methods). FRET *e* was measured as 34 ± 3, 35 ± 4, 41 ± 5, and 22 ± 2% for $P2X_2$-C/Y ($n$ = 31), $\alpha_4$-Y/$\beta_2$-C ($n$ = 17), $\alpha_4$-C/$\beta_2$-Y ($n$ = 16), and $P2X_2$-C/$\alpha_4\beta_2$-Y channels ($n$ = 22), respectively (Fig. 4*B*).

As discussed above (see Materials and Methods) it is necessary to photodestroy the acceptor rapidly for TIRF experiments, so as to minimize distortion by channels outside the evanescent field diffusing into the footprint. We could achieve this photodestruction readily within ~10–30 s (see Materials and Methods) (Figs. 3*B*, 4*A*). However, with this approach, we were restricted to estimating FRET from a single time point (Fig. 4*A*), and we next sought to address the issue of whether measurements of FRET *e* from a single point are reliable compared with measurements of FRET *e* from several points. This was not possible for TIRF, because of the necessity for rapid acceptor photodestruction (see Materials and Methods), but was possible for epifluorescence experiments when the whole cell, rather than the footprint alone, was illuminated. For these experiments, we estimated FRET *e* from linear plots derived from a single point when the acceptor was ~85% destroyed (as in the TIRF experiments) (Fig. 4*A*) and compared these values with FRET *e* estimates derived from linear plots such as those illustrated in Figure 2*B* using multiple points. We performed this analysis for six sets of constructs. Figure 4*C* shows near equality between FRET *e* estimates determined from a single point and those determined for the same constructs with multiple points. This indicates that the measurement of FRET *e* from a single point, when the acceptor is ~85% photodestroyed, provides a reliable measure of true FRET *e*. Moreover, for our most complete data set ($P2X_2$-C/$P2X_2$-Y channels), the FRET *e* estimates determined with TIRF at a single time point (34 ± 3%; $n$ = 31), epifluorescence with five time points (28 ± 8%; $n$ = 7), epifluorescence with one time point (28 ± 8%; $n$ = 7), or linear unmixing [33 ± 5%; $n$ = 18 from Fisher et al. (2004)] were not significantly different. These data indicate that the technical necessity to estimate FRET from a single time point for the TIRF experiments (Fig. 4*A*) does not underestimate or overestimate FRET efficiency. These data and analysis give us confidence in the TIRF data presented in Figure 4*A*.

### FRET between $P2X_2$ and $\alpha_4\beta_2$ channels in neurons

$P2X_2$ and $\alpha_4\beta_2$ channels are endogenously expressed in brain neurons (Kanjhan et al., 1999; Labarca et al., 2001; Fonck et al., 2003), and we next determined whether $P2X_2$ and $\alpha_4\beta_2$ channels undergo FRET when transfected into hippocampal neurons. We measured marked colocalization between $P2X_2$-C/$P2X_2$-Y, $\alpha_4$-C/$\beta_2$-Y, and between $P2X_2$-C and $\alpha_4\beta_2$-Y channels in hippocampal neuron somata (supplemental Fig. 1, available at www.jneurosci.org as supplemental material), as well as strong FRET between $P2X_2$ and $\alpha_4\beta_2$ channels in hippocampal neuron membrane and in whole-cell ROIs (Table 1, Fig. 5*A*). This provides strong evidence that the FRET measured between $P2X_2$ and $\alpha_4\beta_2$ channels in HEK cells also occurs when the subunits are coexpressed in neurons that normally express these channel types (Kanjhan et al., 1999; Labarca et al., 2001; Fonck et al., 2003).

We repeated these experiments for ventral midbrain neurons, which also endogenously express $P2X_2$ and $\alpha_4\beta_2$ channels (Kanjhan et al., 1999; Labarca et al., 2001; Fonck et al., 2003). We measured strong colocalization between CFP- and YFP-labeled $P2X_2$ channel subunits and between CFP- and YFP-labeled $\alpha_4$ and $\beta_2$ subunits but weak colocalization between $P2X_2$-C and $\alpha_4\beta_2$-Y channels (supplemental Fig. 2, available at www.jneurosci.org as supplemental material). Moreover, within midbrain neuron somata, we measured robust FRET for $P2X_2$-C/$P2X_2$-Y and $\alpha_4$-Y/$\beta_2$-C channels ($e$ = 38 ± 8%, $n$ = 4; and 24 ± 6%, $n$ = 3, respectively), but 0% FRET for $P2X_2$-C and $\alpha_4/\beta_2$-Y channels (Fig. 5*C*) ($n$ = 5). These data suggest that there is no interaction between $P2X_2$ and $\alpha_4\beta_2$ channels in midbrain neuron somata, consistent with their distinctly weak colocalization (supplemental Fig. 2, available at www.jneurosci.org as supplemental material). Data for dendrites followed a similar pattern: we measured strong FRET for dendritic $P2X_2$-C/$P2X_2$-Y and $\alpha_4$-Y/$\beta_2$-C channels at 36 ± 5% ($n$ = 7) and 27 ± 4% ($n$ = 4), but 0% FRET for dendritic $P2X_2$-C and $\alpha_4/\beta_2$-Y channels ($n$ = 7). The FRET differences between hippocampal and midbrain neurons extend previous functional studies suggesting that interactions between P2X and nicotinic channels may vary depending on the neuron type (Nakazawa, 1994; Rogers et al., 1997).

### On the percentage of $P2X_2$ and $\alpha_4\beta_2$ channels within 100 Å of each other

Table 1 shows that FRET *e* was lower for whole cells compared with membrane ROI, in agreement with previous data (Nashmi et al., 2003; Fisher et al., 2004). If one assumes that channels in the plasma membrane display a maximal FRET *e* equal to that determined with our highest resolution experiments (TIRF microscopy) and also that unassembled subunits do not FRET because their separation greatly exceeds the Förster distance for CFP and YFP (5 nm; see Materials and Methods), the percentage of fluo-

**Table 1. Average data for FRET efficiency and a measure of channels within 100 Å of each other when expressed in HEK cells and hippocampal neurons**

| | FRET efficiency (%) | | | Channels within 100 Å (%) | | |
|---|---|---|---|---|---|---|
| HEK cells | Membrane | Whole cell | $p < 0.05$ | Membrane | Whole cell | *n* |
| $P2X_2$-C/$P2X_2$-Y | 28 ± 8 | 12 ± 1 | Y | 72 ± 23 | 23 ± 3 | 7 |
| $\alpha_4$-Y/$\beta_2$-C | 25 ± 3 | 17 ± 2 | Y | 77 ± 13 | 37 ± 6 | 9 |
| $\alpha_4$-C/$\beta_2$-Y | 34 ± 3 | 19 ± 3 | Y | 77 ± 8 | 38 ± 6 | 6 |
| $P2X_2$-C, $\alpha_4\beta_2$-Y | 26 ± 3 | 8 ± 2 | Y | 108 ± 16 | 28 ± 13 | 8 |
| $P2X_2$-Y, $\alpha_4$-Y$\beta_2$-C | 23 ± 6 | 8 ± 2 | Y | 93 ± 27 | 30 ± 12 | 6 |
| $P2X_2$-C, $\alpha_4$-Y$\beta_2$[a] | <10[a] | 0 | – | 0 | 0 | 7–14 |
| $P2X_2$-Y, $\alpha_4$-C$\beta_2$ | 0 | 0 | – | 0 | 0 | 6 |
| $P2X_2$-C, $\beta_2$-Y* | 4 ± 4* | 3 ± 2* | – | 0 | 0 | 9 |
| $P2X_6$-C/$P2X_6$-Y | 0 | ~4 | – | 0 | 0 | 9 |
| Hippocampal neurons | | | | | | |
| $P2X_2$-C/$P2X_2$-Y | 19 ± 2 | 21 ± 3 | N | 39 ± 2 | 50 ± 10 | 8–9 |
| $\alpha_4$-C/$\beta_2$-Y | 19 ± 4 | 14 ± 1 | N | 39 ± 10 | 25 ± 3 | 5–7 |
| $P2X_2$-C, $\alpha_4\beta_2$-Y | 22 ± 6 | 11 ± 2 | N | 85 ± 30 | 34 ± 9 | 4–6 |

*Not significantly different from 0%. A value of 0 for FRET efficiency means that linear regressions were not possible for average data or those gathered from single cells. – Indicates that these statistical comparisons could not be performed.
[a]The value of 10% for these experiments is an estimate based on the average data, as shown in Figure 2. N, NO; Y, yes.

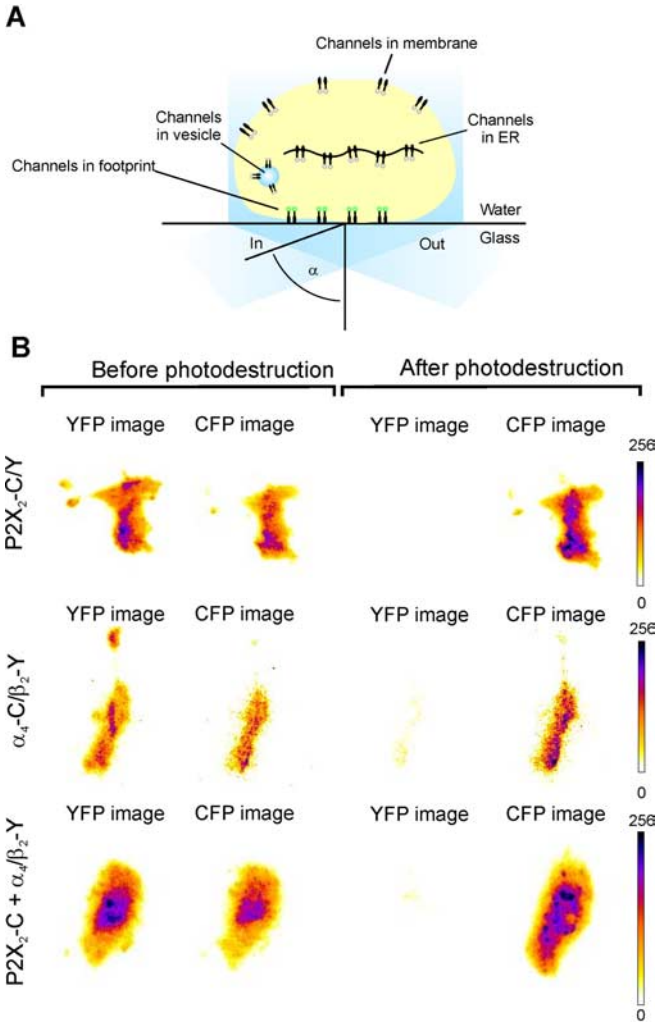


**Figure 3.** FRET measurements for channels within 100 nm of the plasma membrane. ***A***, Diagram of the principle of TIRF microscopy (Steyer and Almers, 2001). Channels within 100 nm of the glass–water interface are strongly optically excited, whereas channels within intracellular compartments and vesicles are not. This restricts FRET measurements to within ~100 nm of the plasma membrane. ***B***, Donor and acceptor images of HEK cell footprints expressing $P2X_2$-C/$P2X_2$-Y (top), $\alpha_4$-C/$\beta_2$-Y (middle), and $P2X_2$ and $\alpha_4\beta_2$-Y (bottom) channels before and after photodestruction of the acceptor fluorophore. Note that clear intensity increases in the CFP images when the acceptor was photodestroyed.

rescent channels that are within ~100 Å (Nashmi et al., 2003) can be calculated as follows:

$$\text{channels within 100 Å (\%)} = (1/e_{\text{TIRF}})(e_{\text{ROI}} - e_{\text{noise}}) \times 100\,, \quad (6)$$

where $e_{\text{TIRF}}$ is the FRET efficiency determined with TIRF, $e_{\text{ROI}}$ is the value for FRET from an ROI (membrane or whole cell) from epifluorescence microscopy and $e_{\text{noise}}$ is the contribution of noise to the FRET measurements. We determined $e_{\text{noise}}$ from experiments with $P2X_6$-C/$P2X_6$-Y channels, because these are unassembled (Torres et al., 1999a) and not functionally expressed in the plasma membrane (Khakh et al., 1999). We calculated a FRET value of 3.5% for $P2X_6$-C/$P2X_6$-Y channels for whole-cell ROIs from the average data, because it was not possible to calculate FRET *e* for all of the single cells, some of which showed negligible photorecovery (Fig. 6). The low FRET value implies that $P2X_6$ channels are expressed mainly as unassembled monomers, a suggestion consistent with previous biochemical experiments (Torres et al., 1999a). From the perspective of the present study, these data thus provide a measure of noise that may arise because of "nonspecific" FRET between subunits that occasionally pass within ~80 Å of each other when coexpressed in cells (Fig. 6, Table 1). This value, 3.5%, is significantly lower than the FRET measurements for $P2X_2$, $\alpha_4\beta_2$, or $P2X_2/\alpha_4\beta_2$ channels (Table 1). Using equation 1, we calculated the percentage of fluorophore-labeled channels that were within ~100 Å of one another for $P2X_2$, $\alpha_4\beta_2$, and $P2X_2/\alpha_4\beta_2$ channels in HEK cells and hippocampal neurons (Table 1). This value was generally higher for $P2X_2$, $\alpha_4\beta_2$, and $P2X_2/\alpha_4\beta_2$ channels in the membrane than for whole cells (Table 1), consistent with the suggestion that whole-cell ROIs contain contributions from the endoplasmic reticulum, which contain a proportion of unassembled channels (Nashmi et al., 2003; Fisher et al., 2004). We suggest that ~30 and ~100% of whole-cell and plasma-membrane channels formed by coexpressing $P2X_2$ and $\alpha_4\beta_2$ channels in HEK cells are dimers between these channel types, with an arrangement such that the $P2X_2$ subunit is ≥80–100 Å from the $\alpha_4$ subunit, but within ~60 Å of the $\beta_2$ subunit (Fig. 7) (see Materials and Methods and Discussion).

## Discussion

The main finding, summarized diagrammatically in Figure 7, is that $P2X_2$ and $\alpha_4\beta_2$ channels form a molecular scale partnership within 100 nm of the plasma membrane.

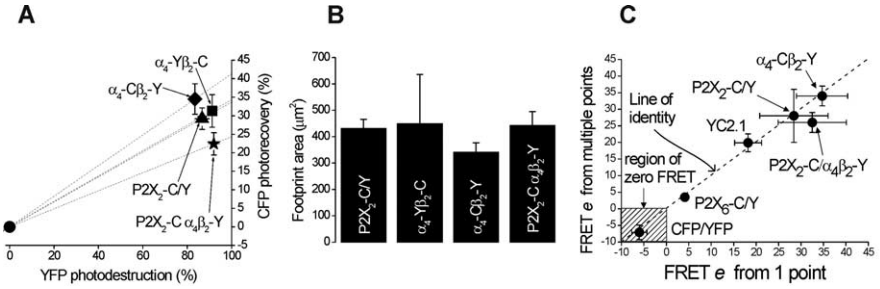


**Figure 4.** FRET estimates from TIRF microscopy. ***A***, Linear plots of donor (CFP) photorecovery versus acceptor (YFP) photodestruction for channels formed by coexpressing the indicated subunits. The *y*-axis intercept is a measure of FRET *e* (see Materials and Methods, Data analysis). ***B***, Footprint areas for the cells shown in ***A***. ***C***, A comparison of FRET *e* values determined from a single point or for multiple points with epifluorescence microscopy (as in Fig. 2). The data for cytosolic CFP and YFP (CFP/YFP) and yellow cameleon 2.1 (YC2.1) determined with multiple points have been reported (Fisher et al., 2004). The data point for $P2X_6$ has no error bars, because we could estimate FRET *e* only from the average data (see Results). Error bars represent SEM.

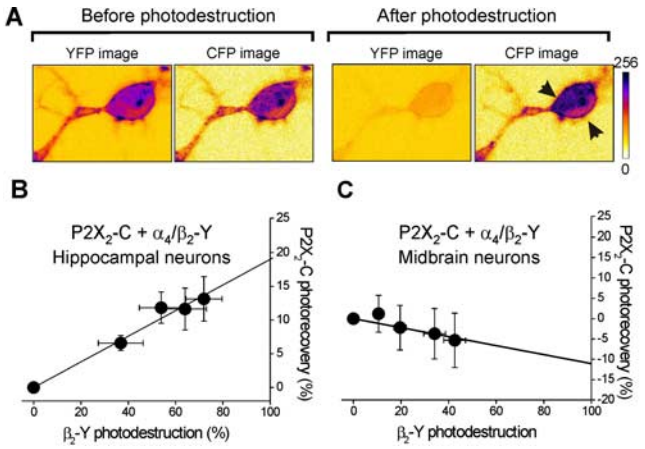


**Figure 5.** FRET for channels expressed in hippocampal and midbrain neurons. ***A***, Representative donor and acceptor images of a hippocampal neuron expressing $P2X_2$-C/$P2X_2$-Y channels before and after photodestruction of the acceptor fluorophore. ***B***, Linear plots of donor (CFP) photorecovery versus acceptor (YFP) photodestruction for channels formed by coexpressing $P2X_2$-C and $P2X_2$-Y channels in hippocampal neurons. The *y*-axis intercept is equal to FRET *e*. ***C***, As in ***B*** but for subunits coexpressed in ventral midbrain neurons.

### Functional and optical measures of an interaction between $P2X_2$ and $\alpha_4\beta_2$ channels

The electrophysiological data for $P2X_2$ and $\alpha_4\beta_2$ channels expressed in HEK cells demonstrate that these channels undergo functional interactions similar to those described previously for $P2X_2$ and nicotinic, GABA, or 5-$HT_3$ channels (Nakazawa, 1994; Barajas-Lopez et al., 1998; Searl and Silinsky, 1998; Searl et al., 1998; Zhou and Galligan, 1998; Khakh et al., 2000; Sokolova et al., 2001b; Barajas-Lopez et al., 2002; Boue-Grabot et al., 2003, 2004a,b). In future work, it will be important to test whether cross-inhibition also occurs for P2X and nicotinic channels in brain neuron nerve terminals, where they are often coexpressed (Kanjhan et al., 1999; MacDermott et al., 1999; Khakh and Henderson, 2000; Labarca et al., 2001; Fonck et al., 2003; Engelman and MacDermott, 2004). Indeed, there is evidence that some P2X-like channels colocalize and display cross-inhibition with nicotinic channels within cholinergic nerve terminals (Diaz-Hernandez et al., 2002, 2004).

Interestingly, we found robust FRET between $P2X_2$ and $\alpha_4\beta_2$ channels in hippocampal neurons but not in midbrain neurons. Neuron-specific interactions also occur in the periphery: cross-inhibition occurred in sympathetic neurons from the celiac ganglion (Searl et al., 1998) but not in those from the superior cervical ganglion (Rogers et al., 1997). Perhaps there are neuron-specific cues that govern cross-inhibition, for example variable expression of interacting or targeting proteins.

We proposed previously that conformational spread may explain the ability of $P2X_2$ and nicotinic channels to display cross-inhibition (Khakh et al., 2000). In the simplest cases, the proteins that display conformational spread are spatially close or linked (Bray and Duke, 2004) so that motions in a molecule are communicated to its neighbors. Conformational spread is well studied for bacterial chemotaxis and may also occur for receptors and channels (Bray and Duke, 2004). However, there have been no data on the spatial arrangement or possible physical association of $P2X_2$ and nicotinic channels in the plasma membrane, a prerequisite for conformational spread. The present study provides FRET-based evidence for an angstrom scale interaction between full-length $P2X_2$ and $\alpha_4\beta_2$ nicotinic channels in the plasma membrane of living cells. Thus, we complement previous electrophysiological studies on cross-inhibition. The FRET measurements imply that $P2X_2$ interacts more strongly with the $\beta_2$ than with the $\alpha_4$ nicotinic receptor subunit and provide the percentage of channels that are within ~100 Å of each other and also within 100 nm of the plasma membrane (Fig. 7*B*).

### Molecular interpretations of FRET efficiency data

It is unlikely that the FRET data reported here arise from a nonspecific phenomenon such as "overcrowding in the membrane." First, FRET for P2X channels depends strongly on the subunit combination: $P2X_6$ shows negligible FRET (0–3.5%), $P2X_1$ displays intermediate FRET (19%), and $P2X_2$ shows the highest FRET (30–35%) (this study and Fisher et al., 2004). Importantly, all these subunits express robustly in HEK cells (Torres et al., 1999a; North, 2002) and yet FRET varies by a factor of 10. This is inconsistent with simple overcrowding causing FRET in our experiments. Second, previous experiments show that FRET is specific to heteromeric $\alpha_4\beta_2$ channels or to heteromeric GluCl channels and does not occur between nicotinic or GluCl subunits when they are expressed in the same cell (Nashmi et al., 2003), also arguing against overcrowding. Likewise, in this study, FRET for $\alpha_4\beta_2$ channels varied depending on the $\alpha$:$\beta$ ratio, as expected of preferential donor/acceptor ratios (2:3 vs 3:2), arguing against overcrowding phenomena. Third, FRET between $P2X_2$ and $\alpha_4\beta_2$ channels was specific, occurring only between $P2X_2$ and $\beta_2$ subunits in $\alpha_4\beta_2$ channels. If FRET occurred because of overcrowding, it would presumably not discriminate between $\alpha_4$ and $\beta_2$ subunits in assembled $\alpha_4\beta_2$ channels. Fourth, we measured no FRET in cells expressing $P2X_2$ and $\beta_2$ subunits alone. Fifth, direct imaging shows that $P2X_2$ channels do not form clusters of overcrowded receptors but rather adopt a relatively uniform membrane distribution (Khakh and Egan, 2005). Sixth, both $P2X_2$ and $\alpha_4\beta_2$ channels are expressed at a density of $<10$ channels/$\mu m^2$ (Khakh et al., 2001; Nashmi et al., 2003; Fisher et al., 2004; Fujiwara and Kubo, 2004; Khakh and Egan, 2005). In contrast, channels become crowded at plasma membrane densities $>10{,}000$ channels/$\mu m^2$ (Hille, 2001). Seventh, FRET has been used for

decades to measure protein–protein interactions; no substantive data or arguments question the validity of the approach because of nonspecific overcrowding in the membrane (Michalet et al., 2003; Bunt and Wouters, 2004). Future work may overcome the technical challenges of systematically varying the expression levels of $P2X_2$ and $\alpha_4\beta_2$ channels and determine the impact on FRET.

The FRET efficiency values for $P2X_2$ and $\alpha_4\beta_2$ channels reported here agree with previous estimates (Nashmi et al., 2003; Fisher et al., 2004) and in the case of nicotinic channels with values expected from a 4.6 Å structural model (Miyazawa et al., 1999). Extrapolating from this model to $\alpha_4\beta_2$ channels (Fig. 7*A*) suggests that the distance between the edges of any $\alpha_4$ subunit and its nearest or farthest $\beta_2$ subunit would be ~38 Å (a) or ~45 Å (b), respectively. Note that the fluorophore is buried in a $\beta$-can ~30 Å in diameter and ~45 Å in length (Tsien, 1998). Assuming that the fluorescent protein domains line up with their long axes parallel, this implies that the surfaces of the two fluorescent protein domains are separated in $\alpha_4\beta_2$ channels by ~60 minus ~30 Å (from two fluorophore radii) or ~30 Å. We consider this probable because the five fluorophores likely stick out from the helices forming the $\alpha_4\beta_2$ cytosolic domain rather than being buried within them, which we presume would be detrimental given the relatively small dimensions of, and available space within, the entire domain (Miyazawa et al., 1999). Because of the $1/R^6$ dependence, the estimate of ~30 Å measures primarily the distance *a* between an $\alpha_4$ subunit and its nearest $\beta_2$ (Fig. 7*A*). Finally, if the 2:3 $\alpha$:$\beta$ stoichiometry and arrangement of Figure 7 is correct, $J_{DA}$ is effectively doubled, and the value of ~30 Å is an underestimate by ~12%. Thus, the experiments suggest a distance estimate for $\alpha_4\beta_2$ channels at ~33 Å, comparable with 39–41 Å expected from a structural model of a related channel. Similar comparisons are not possible for P2X channels, because no structural models exist, but the FRET efficiency measurements agree roughly with expectations from structural models of the cytosolic domains of several ion channels (Chang et al., 1998; Miyazawa et al., 1999; Sokolova et al., 2001a; Higgins et al., 2002; Jiang et al., 2002; da Fonseca et al., 2003; Kuo et al., 2003).

The finding that FRET is ~30–34% for $P2X_2$ channels and ~3.5% for $P2X_6$ channels provides strong evidence that FRET efficiency for P2X channels is subunit specific. In previous data, $P2X_1$ channels display intermediate FRET efficiency at ~19% (Fisher et al., 2004). The difference for FRET between probes at the extreme C terminus of $P2X_2$ and $P2X_1$ channels may arise because $P2X_2$ channels have a longer C terminus (120 residues) compared with $P2X_1$ (47 residues); perhaps the $P2X_2$ cytosolic domain resembles a phonograph needle, with the C terminus at the cytoplasmic tip (Fisher et al., 2004). The value of 3.5% represents an upper limit and probably measures noise in our experiments; FRET for $P2X_6$ channels may not exist, consistent with electrophysiological (Le et al., 1998; Khakh et al., 1999), biochemical (Torres et al., 1999a), and atomic force microscopy studies (Barrera et al., 2005) demonstrating that $P2X_6$ subunits do not oligomerize but remain as unassembled monomers. In contrast, $P2X_2$ subunits apparently assemble as trimers (Aschrafi et al., 2004; Barrera et al., 2005). We are encouraged that FRET imaging experiments on several thousand channels in single living cells provide information consistent with biochemistry and atomic force microscopy on concentrated, isolated, and purified channels. FRET may take its place as a noninvasive approach to understand the molecular basis and dynamics of P2X channel assembly and trafficking (Torres et al., 1999a,b; Chaumont et al., 2004).

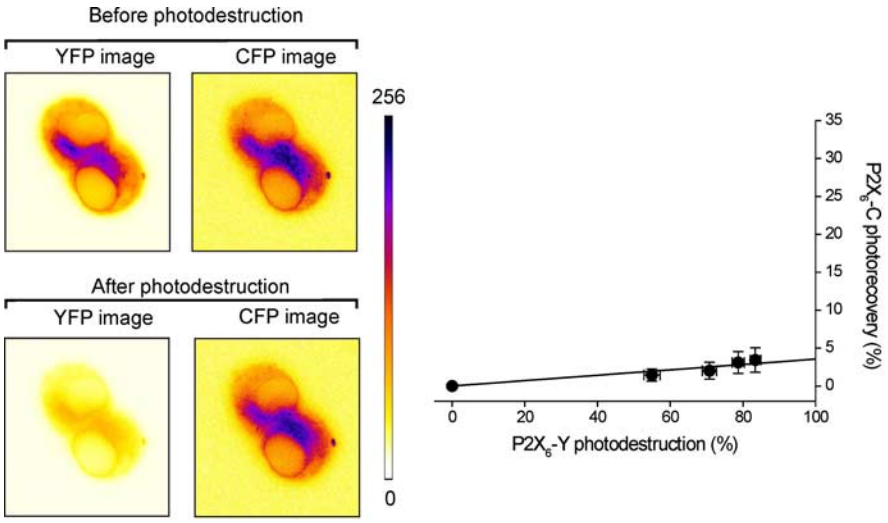


**Figure 6.** FRET after coexpression of CFP and YFP-labeled $P2X_6$ subunits. ***A***, Donor (CFP) and acceptor (YFP) images of two HEK cells expressing $P2X_6$-C/$P2X_6$-Y subunits before and after photodestruction of the acceptor fluorophore. Note the minimal dequenching of the donor. ***B***, Linear plots of donor (CFP) photorecovery versus acceptor (YFP) photodestruction for channels formed by coexpressing $P2X_6$ subunits. The *y*-axis intercept is equal to FRET *e* (see Materials and Methods, Data analysis).

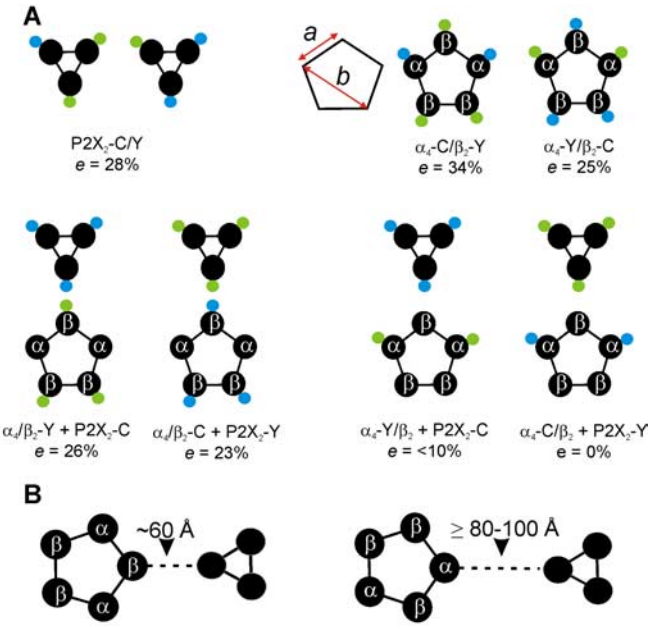


**Figure 7.** Diagrams summarizing FRET data. ***A***, Summary of the FRET efficiency values determined with epifluorescence FRET imaging for membrane ROI. The blue and yellow dots represent CFP and YFP, respectively. The pentagon illustrates the shortest (a) and longest (b) straight line distances between $\alpha$ and $\beta$ subunits. ***B***, The diagrams illustrate the salient findings, namely that $P2X_2$ is within 60 Å of the $\beta_2$ subunit in $\alpha_4\beta_2$ channels and >80 Å from the $\alpha_4$ subunit. By drawing the channels parallel to one another, we are not making any statements about their three-dimensional relationships to each other but rather schematically illustrating the key findings from FRET.

### The interpretation of FRET efficiencies

Several uncertainties arise when one interprets FRET in terms of absolute distance. (1) We assume that the fluorophores adopt random orientations, so that the assumed orientation factor $\kappa^2 = 2/3$ implies that $R_0 = 50$ Å (see Materials and Methods). (2) In the case of trimeric $P2X_2$ channels (Fig. 7*A*), it is important to note that 50% of the channels that undergo FRET have two donors and one acceptor, and 50% have one donor and two acceptors (Fisher et al., 2004). Fluorescence lifetime measurements might discriminate between these populations; however, in the absence of such experiments, our data likely represent an average of the FRET efficiencies from these different donor/acceptor ratios (Fig. 7*A*). (3) In $\alpha_4\beta_2$ nicotinic channels, the fluorophore is embedded in M3–M4 intracellular loops of varying length, and presumably size, among subunits ($\alpha_4$, 271 aa; $\beta_2$, 138 aa), which is expected to produce asymmetry. (4) $\alpha_4\beta_2$ nicotinic channels are pentamers, with variable stoichiometry of $\alpha_4$ to $\beta_2$ subunits rather than the fixed 2:3 $\alpha$:$\beta$ of Figure 7, and therefore unknown donor/acceptor ratios in our experiments (Zwart and Vijverberg, 1998; Nelson et al., 2003). These quantitative uncertainties do not vitiate the qualitative finding that FRET was robust and high for $P2X_2$ and $\beta_2$ subunits (Fig. 7*A*) and negligible between $P2X_2$ and $\alpha_4$ subunits (Fig. 7*A*), indicating a strongly preferential order of subunits in a spatial arrangement encompassing $P2X_2$ and $\alpha_4\beta_2$ channels (Fig. 7*B*).

### Summary and outlook

That structurally distinct transmitter-gated channels can form plasma membrane partnerships extends previous work on assembly of dopamine and somatostatin (Rocheville et al., 2000), adenosine (Gines et al., 2000), $GABA_A$ (Liu et al., 2000), and NMDA (Lee et al., 2002) receptors. Thus, functional interactions between structurally distinct receptors and channels may be a general mechanism. The finding that the $P2X_2$ C terminus interacts specifically in living cells with the cytosolic domain of distinct subunits from the Cys-loop channel family is consistent with biochemical studies on interactions between $P2X_2$ and GABA-gated ion channels (Boue-Grabot et al., 2004a,b). The close spatial apposition of $P2X_2$ and $\alpha_4\beta_2$ channel cytosolic domains may be sufficient to allow state-dependent conformational spread from one receptor to its neighbor (Bray and Duke, 2004).

## References


Aschrafi A, Sadtler S, Niculescu C, Rettinger J, Schmalzing G (2004) Trimeric architecture of homomeric P2X(2) and heteromeric P2X(1+2) receptor subtypes. J Mol Biol 342:333–343.

Barajas-Lopez C, Espinosa-Luna R, Zhu Y (1998) Functional interactions between nicotinic and P2X channels in short-term cultures of guinea-pig submucosal neurons. J Physiol (Lond) 513:671–683.

Barajas-Lopez C, Montano LM, Espinosa-Luna R (2002) Inhibitory interactions between 5-HT3 and P2X channels in submucosal neurons. Am J Physiol Gastrointest Liver Physiol 283:G1238–G1248.

Barrera NP, Ormond SJ, Henderson RM, Murrell-Lagnado RD, Edwardson JM (2005) Atomic force microscopy imaging demonstrates that P2X2 receptors are trimers but that P2X6 receptor subunits do not oligomerize. J Biol Chem 280:10759–10765.

Boue-Grabot E, Barajas-Lopez C, Chakfe Y, Blais D, Belanger D, Emerit MB, Seguela P (2003) Intracellular cross talk and physical interaction between two classes of neurotransmitter-gated channels. J Neurosci 23:1246–1253.

Boue-Grabot E, Emerit MB, Toulme E, Seguela P, Garret M (2004a) Cross-talk and co-trafficking between rho1/GABA receptors and ATP-gated channels. J Biol Chem 279:6967–6975.

Boue-Grabot E, Toulme E, Emerit MB, Garret M (2004b) Subunit specific coupling between GABA type A and P2X2 receptor channels. J Biol Chem 279:52517–52525.

Bray D, Duke T (2004) Conformational spread: the propagation of allosteric states in large multiprotein complexes. Annu Rev Biophys Biomol Struct 33:53–73.

Bunt G, Wouters FS (2004) Visualization of molecular activities inside living cells with fluorescent labels. Int Rev Cytol 237:205–277.

Chang G, Spencer RH, Lee AT, Barclay MT, Rees DC (1998) Structure of the MscL homolog from Mycobacterium tuberculosis: a gated mechanosensitive ion channel. Science 282:2220–2226.

Chaumont S, Jiang LH, Penna A, North RA, Rassendren F (2004) Identification of a trafficking motif involved in the stabilization and polarization of P2X receptors. J Biol Chem 279:29628–29638.

Chavez-Noriega LE, Gillespie A, Stauderman KA, Crona JH, Claeps BO, Elliot KJ, Reid RT, Rao TS, Velicelebi G, Hapold MM, Johnson EC, Corey-Naeve J (2000) Characterization of the recombinant human neuronal nicotinic acetylcholine receptors alpha3beta2 and alpha4beta2 stably expressed in HEK 293 cells. Neuropharmacology 39:2543–2560.

da Fonseca PC, Morris SA, Nerou EP, Taylor CW, Morris E, P (2003) Domain organization of the type 1 inositol 1,4,5-trisphosphate receptor as revealed by single-particle analysis. Proc Natl Acad Sci USA 100:3936–3941.

Diaz-Hernandez M, Pintor J, Castro E, Miras-Portugal MT (2002) Colocalisation of functional nicotinic and ionotropic nucleotide receptors in isolated cholinergic synaptic terminals. Neuropharmacology 42:20–33.

Diaz-Hernandez M, Sanchez-Nogueiro J, Pintor J, Miras-Portugal MT (2004) Interaction between dinucleotide and nicotinic receptors in individual cholinergic terminals. J Pharmacol Exp Ther 311:954–967.

Dickinson ME, Bearman G, Tille S, Lansford R, Fraser SE (2001) Multispectral imaging and linear unmixing add a whole new dimension to laser scanning fluorescence microscopy. Biotechniques 31:1272, 1274–1276, 1278.

Egan TM, Khakh BS (2004) Contribution of calcium ions to P2X channel responses. J Neurosci 24:3413–3420.

Egan TM, Haines WR, Voigt MM (1998) A domain contributing to the ion channel of ATP-gated $P2X_2$ receptors identified by the substituted cysteine accessibility method. J Neurosci 18:2350–2359.

Engelman HS, MacDermott AB (2004) Presynaptic ionotropic receptors and control of transmitter release. Nat Rev Neurosci 5:135–145.

Fisher JA, Girdler G, Khakh BS (2004) Time resolved measurement of state specific P2X ion channel cytosolic gating motions. J Neurosci 24:10475–10487.

Fonck C, Nashmi R, Deshpande P, Damaj MI, Marks MJ, Riedel A, Schwarz J, Collins AC, Labarca C, Lester HA (2003) Increased sensitivity to agonist-induced seizures, straub tail, and hippocampal theta rhythm in knock-in mice carrying hypersensitive $\alpha$4 nicotinic receptors. J Neurosci 23:2582–2590.

Fujiwara Y, Kubo Y (2004) Density-dependent changes of the pore properties of the P2X2 receptor channel. J Physiol (Lond) 558:31–43.

Gines S, Hillion J, Torvinen M, Le Crom S, Casado V, Canela E, Rondin S, Lew JY, Watson S, Zoli M, Agnati LF, Verniera P, Lluis C, Ferre S, Fuxe K, Franco R (2000) Dopamine D1 and adenosine A1 receptors form functionally interacting heteromeric complexes. Proc Natl Acad Sci USA 97:8606–8611.

Green T, Heinemann SF, Gusella JF (1998) Molecular neurobiology and genetics: investigation of neural function and dysfunction. Neuron 20:427–444.

Higgins MK, Weitz D, Warne T, Schertler GF, Kaupp UB (2002) Molecular architecture of a retinal cGMP-gated channel: the arrangement of the cytoplasmic domains. EMBO J 21:2087–2094.

Hille B (2001) Ion channels of excitable membranes, Chap 12, Ed 3. Sunderland, MA: Sinauer Associates.

Jiang Y, Lee A, Chen J, Cadene M, Chait BT, MacKinnon R (2002) Crystal structure and mechanism of a calcium-gated potassium channel. Nature 417:515–522.

Kanjhan R, Housley GD, Burton LD, Christie DL, Kippenberger A, Thorne PR, Luo L, Ryan AF (1999) Distribution of the P2X2 receptor subunit of the ATP-gated ion channels in the rat central nervous system. J Comp Neurol 407:11–32.

Khakh BS (2001) Molecular physiology of P2X receptors and ATP signalling at synapses. Nat Rev Neurosci 2:165–174.

Khakh BS, Egan TM (2005) Contribution of transmembrane regions to ATP-gated P2X2 channel permeability dynamics. J Biol Chem 280:6118–6129.

Khakh BS, Henderson G (2000) Modulation of fast synaptic transmission by presynaptic ligand-gated cation channels. J Auton Nerv Syst 81:110–121.

Khakh BS, Proctor WR, Dunwiddie TV, Labarca C, Lester HA (1999) Allosteric control of gating and kinetics at $P2X_4$ receptor channels. J Neurosci 19:7289–7299.

Khakh BS, Zhou X, Sydes J, Galligan JJ, Lester HA (2000) State-dependent cross-inhibition between transmitter-gated cation channels. Nature 406:405–410.

Khakh BS, Smith WB, Chiu CS, Ju D, Davidson N, Lester HA (2001) Activation-dependent changes in receptor distribution and dendritic morphology in hippocampal neurons expressing P2X2-green fluorescent protein receptors. Proc Natl Acad Sci USA 98:5288–5293.

Kuo A, Gulbis JM, Antcliff JF, Rahman T, Lowe ED, Zimmer J, Cuthbertson J, Ashcroft FM, Ezaki T, Doyle DA (2003) Crystal structure of the potassium channel KirBac1.1 in the closed state. Science 300:1922–1926.

Labarca C, Schwarz J, Deshpande P, Schwarz S, Nowak MW, Fonck C, Nashmi R, Kofuji P, Dang H, Shi W, Fidan M, Khakh BS, Chen Z, Bowers BJ, Boulter J, Wehner JM, Lester HA (2001) Point mutant mice with hypersensitive alpha 4 nicotinic receptors show dopaminergic deficits and increased anxiety. Proc Natl Acad Sci USA 98:2786–2791.

Lansford R, Bearman G, Fraser SE (2001) Resolution of multiple green fluorescent protein color variants and dyes using two-photon microscopy and imaging spectroscopy. J Biomed Opt 6:311–318.

Le KT, Babinski K, Séguéla P (1998) Central $P2X_4$ and $P2X_6$ channel subunits coassemble into a novel heteromeric ATP receptor. J Neurosci 18:7152–7159.

Lee FJ, Xue S, Pei L, Vukusic B, Chery N, Wang Y, Wang YT, Niznik HB, Yu XM, Liu F (2002) Dual regulation of NMDA receptor functions by direct protein-protein interactions with the dopamine D1 receptor. Cell 111:219–230.

Lester HA, Dibas MI, Dahan DS, Leite JF, Dougherty DA (2004) Cys-loop receptors: new twists and turns. Trends Neurosci 27:329–336.

Liu F, Wan Q, Pristupa ZB, Yu X-M, Wang YT, Niznik HB (2000) Direct protein-protein coupling enables cross-talk between dopamine D5 and g-aminobutyric acid A receptors. Nature 403:274–280.

MacDermott AB, Role LW, Siegelbaum SA (1999) Presynaptic ionotropic receptors and the control of transmitter release. Annu Rev Neurosci 22:443–485.

Michalet X, Kapanidis AN, Laurence T, Pinaud F, Doose S, Pflughoefft M, Weiss S (2003) The power and prospects of fluorescence microscopies and spectroscopies. Annu Rev Biophys Biomol Struct 32:161–182.

Miyazawa A, Fujiyoshi Y, Stowell M, Unwin N (1999) Nicotinic acetylcholine receptor at 4.6 A resolution: transverse tunnels in the channel wall. J Mol Biol 288:765–786.

Nakazawa K (1994) ATP-activated current and its interaction with acetylcholine-activated current in rat sympathetic neurons. J Neurosci 14:740–750.

Nashmi R, Dickinson ME, McKinney S, Jareb M, Labarca C, Fraser SE, Lester HA (2003) Assembly of $\alpha 4\beta 2$ nicotinic acetylcholine receptors assessed with functional fluorescently labeled subunits: effects of localization, trafficking, and nicotine-induced upregulation in clonal mammalian cells and in cultured midbrain neurons. J Neurosci 23:11554–11567.

Nelson ME, Kuryatov A, Choi CH, Zhou Y, Lindstrom J (2003) Alternate stoichiometries of a4b2 nicotinic acetylcholine receptors. Mol Pharmacol 63:332–341.

North RA (1996a) Families of ion channels with two hydrophobic segments. Curr Opin Cell Biol 8:474–483.

North RA (1996b) P2X receptors: a third major class of ligand-gated ion channels. Ciba Found Symp 198:91–105.

North RA (2002) Molecular physiology of P2X receptors. Physiol Rev 82:1013–1067.

Patterson GH, Piston DW, Barisas BG (2000) Forster distances between green fluorescent protein pairs. Anal Biochem 284:438–440.

Riven I, Kalmanzon E, Segev L, Reuveny E (2003) Conformational rearrangements associated with the gating of the G protein-coupled potassium channel revealed by FRET microscopy. Neuron 38:225–235.

Rocheville M, Lange DC, Kumar U, Patel SC, Patel RC, Patel YC (2000) Receptors for dopamine and somatostatin: formation of hetero-oligomers with enhanced functional activity. Science 288:154–157.

Rogers M, Colquhoun LM, Patrick JW, Dani JA (1997) Calcium flux through predominantly independent purinergic ATP and nicotinic acetylcholine receptors. J Neurophysiol 77:1407–1417.

Searl TJ, Silinsky EM (1998) Cross-talk between apparently independent receptors. J Physiol (Lond) 513:629–630.

Searl TJ, Redman RS, Silinsky EM (1998) Mutual occlusion of P2X ATP receptors and nicotinic receptors on sympathetic neurons of the guinea-pig. J Physiol (Lond) 510:783–791.

Shimoda K, Sauve Y, Marini A, Schwartz JP, Commissiong JW (1992) A high percentage yield of tyrosine hydroxylase-positive cells from rat E14 mesencephalic cell culture. Brain Res 586:319–331.

Sokolova O, Kolmakova-Partensky L, Grigorieff N (2001a) Three-dimensional structure of a voltage-gated potassium channel at 2.5 nm resolution. Structure (Camb) 9:215–220.

Sokolova E, Nistri A, Giniatullin R (2001b) Negative cross talk between anionic $GABA_A$ and cationic P2X ionotropic receptors of rat dorsal root ganglion neurons. J Neurosci 21:4958–4968.

Steyer JA, Almers W (2001) A real-time view of life within 100 nm of the plasma membrane. Nat Rev Mol Cell Biol 2:268–275.

Torres G, Egan T, Voigt M (1999a) Hetero-oligomeric assembly of P2X receptor subunits. Specificities exist with regard to possible partners. J Biol Chem 274:6653–6659.

Torres GE, Egan TM, Voigt MM (1999b) Identification of a domain involved in ATP-gated ionotropic receptor subunit assembly. J Biol Chem 274:22359–22365.

Tsien RY (1998) The green fluorescent protein. Annu Rev Biochem 67:509–544.

Zhou X, Galligan JJ (1998) Non-additive interaction between nicotinic cholinergic and P2X purine receptors in guinea-pig enteric neurons in culture. J Physiol (Lond) 513:685–697.

Zwart R, Vijverberg HP (1998) Four pharmacologically distinct subtypes of a4b2 nicotinic acetylcholine receptor expressed in *Xenopus laevis* oocytes. Mol Pharmacol 54:1124–1131.